Shock remanent magnetization intensity and stability structures of single-domain titanomagnetite-bearing basalt sample

Masahiko Sato[1], Kosuke Kurosawa[2], Shota Kato[1], Masashi Ushioda[3], and Sunao Hasegawa[4]

[1]The University of Tokyo
[2]Chiba Institute of Technology
[3]Shikoku Research Institute Inc.
[4]Japan Aerospace Exploration Agency

November 22, 2022

Abstract

Knowledge of the shock remanent magnetization (SRM) structure is crucial to interpret the spatial changes in magnetic anomalies observed over the impact crater. This study reports the SRM intensity and stability structures of single-domain titanomagnetite-bearing basalt based on the SRM acquisition experiments, remanence measurements for divided subsamples, and impact simulations. The SRM properties systematically change with increasing pressure, and three distinctive aspects are recognized at different pressure ranges: (1) constant intensity below 0.1 GPa, (2) linear trend as intensity is proportional to pressure up to 1.1 GPa, and (3) constant intensity and increasing stability above 1.9 GPa. The SRM intensity and stability structures suggest that the crustal rocks containing the single-domain titanomagnetite originally had an SRM intensity structure according to the distance from the impact point, which changed depending on the remanence stability after the impact.

Shock remanent magnetization intensity and stability structures of single-domain titanomagnetite-bearing basalt sample

Masahiko Sato[1]* (m.sato@eps.s.u-tokyo.ac.jp), Kosuke Kurosawa[2], Shota Kato[1], Masashi Ushioda[3], and Sunao Hasegawa[4]

[1]Department of Earth and Planetary Science, The University of Tokyo, Tokyo, Japan

[2]Planetary Exploration Research Center, Chiba Institute of Technology, Narashino, Japan

[3]Department of Civil Engineering, Shikoku Research Institute Inc., Takamatsu, Japan

[4]Institute of Space and Astronautical Science, Japan Aerospace Exploration Agency, Sagamihara, Japan

*Department of Earth and Planetary Science, The University of Tokyo, 7-3-1 Hongo, Bunkyo-ku, Tokyo 113-0033 Japan

Abstract

Knowledge of the shock remanent magnetization (SRM) structure is crucial to interpret the spatial changes in magnetic anomalies observed over the impact crater. This study reports the SRM intensity and stability structures of single-domain titanomagnetite-bearing basalt based on the SRM acquisition experiments, remanence measurements for divided subsamples, and impact simulations. The SRM properties systematically change with increasing pressure, and three distinctive aspects are recognized at different pressure ranges: (1) constant intensity below 0.1 GPa, (2) linear trend as intensity is proportional to pressure up to 1.1 GPa, and (3) constant intensity and increasing stability above 1.9 GPa. The SRM intensity and stability structures suggest that the crustal rocks containing the single-domain titanomagnetite originally had an SRM intensity structure according to the distance from the impact point, which changed depending on the remanence stability after the impact.

1. Introduction

Shock remanent magnetization (SRM) is acquired as a result of the shock wave propagation in a magnetic field (Nagata, 1971). A clear relationship between the formation ages and magnetic anomaly intensities observed over the impact craters on terrestrial planets (e.g., Acuña et al., 1999; Lillis et al., 2008; Mitchell et al., 2008) indicates the SRM acquisition and/or the impact-induced demagnetization of crustal rocks at the time of impact events. The SRM records of impact craters are vital in reconstructing the evolution of the planetary field. Knowledge of a three-dimensional distribution of the SRM intensity is crucial for interpreting the spatial change in magnetic anomalies observed over the crater and reconstructing the paleo-planetary field based on the anomaly data. However, the intensity distribution is an unexplained phenomena concerning SRM properties owing to the lack of subsample magnetization measurements for the experimental SRM-imparted samples.

Investigations of the SRM acquisition and measurement of the whole samples showed that the SRM intensities of the natural basalt, Apollo 12 crystalline rocks (Nagata, 1971), and basalt samples containing both the single-domain (SD) and multidomain (MD) titanomagnetite (Pohl et al., 1975) were proportional to the applied pressure. This suggests that the SRM intensity depends on the location in the shocked samples owing to the variation in the pressure and temperature during the shock propagation. Srnka et al. (1979) conducted an impact-induced SRM acquisition experiment with natural remanent magnetization- (NRM) bearing basalt plate samples containing MD titanomagnetite, and measured the remanence intensities of core samples drilled from the shocked basalt. They qualitatively demonstrated that the SRM intensities decreased with increasing distance from the impact point. Gattacceca et al. (2008) conducted laser-induced SRM acquisition experiments using pseudo-SD (PSD) titanomagnetite-bearing basalt and MD magnetite-bearing microdiorite samples. They cut cylindrical samples that were 10 mm high and 9.5 mm in diameter into parallelepipedic subsamples with a thickness of 1 mm and measured the SRM intensities. The SRM acquisitions were homogeneous in the cylindrical samples, and this was further supported by the superconducting quantum interference device (SQUID) microscope measurement for the SRM-bearing basalt sample (Gattacceca et al., 2010). Although the SRM structure should depend on the composition and magnetic domain state of magnetic minerals, there is no consensus on the SRM structure owing to limited papers, and further investigation is clearly required.

To investigate the SRM intensity and stability structures using a magnetically well-characterized basalt sample bearing fine-grained SD titanomagnetite, we conducted the newly designed SRM acquisition experiments and remanence measurements for cube-shaped subsamples cut from the SRM-imparted samples. The pressure and temperature changes during the shock wave propagation were estimated from the impact simulations. Based on the SRM experiments, remanence measurements, and impact simulations, this study reports the relationships between SRM properties and pressure/temperature changes during the shock wave propagation.

2. Method

2.1 Experimental sample

A natural basalt sample (Linxi, Inner Mongolia) was used for the SRM experiments. The basalt consists of olivine phenocrysts approximately 0.6 mm in diameter and fine-grained plagioclase, clinopyroxene, olivine, glass, and opaque minerals in the groundmass (Figure S1). The NRM intensity of the basalt sample was 7.58×10^{-4} Am^2/kg and decreased to 1.36×10^{-4} Am^2/kg after a stepwise alternating field demagnetization (AFD) treatment of 80 mT (Figure S2). A strong-field thermomagnetic curve shows a Curie temperature (T_C) of 237 ^oC (Figure S3a) and zero-field cooling and field cooling remanence curves of low-temperature remanence measurements show a remanence loss at approximately 60 K (Figure S3b), indicating that Ti-rich titanomagnetite is the main remanence carrier of the basalt sample (Hunt et al., 1995; Moskowitz et al., 1998). The ulvöspinel content x ($Fe_{3-x}Ti_xO_4$) estimated from the T_C value was x = 0.51 (Hunt et al., 1995). Magnetic hysteresis parameters and first-order reversal curves (FORC) indicate the presence of SD grains with slight magnetostatic interactions (Day et al., 1977; Roberts et al., 2000). The titanomagnetite concentration in the basalt samples is estimated as 0.7 wt% using the saturation magnetization values of the magnetic hysteresis loop.

2.2 Shock remanence acquisition experiment

A two-stage light gas gun at the Institute of Space and Astronautical Science (ISAS) of the Japan Aerospace and Exploration Agency (JAXA) was used for the SRM acquisition experiments. A schematic diagram of the experimental system for SRM acquisition is shown in Figure S4. A three-layered magnetic shield with a cylindrical form was set in a vacuum experimental chamber connected to a two-stage light gas gun. The diameter and length of the shield were 32 and 100 cm, respectively. The residual field in the shield was less than 0.3 μT. A solenoid coil with a diameter of 26 cm was placed in the magnetically shielded cylinder.

The basalt samples were shaped into cylinders that were 10 cm both in diameter and length, and used as targets in the SRM acquisition experiments. A cylindrical coordinate system was used to describe the shock remanence. The sample's cylindrical axis and radial directions were defined as the *Z*- and *R*-axes, respectively (Figure S5). The basalt sample was placed at the center of the solenoid coil, and the basalt cylinder, solenoid coil, and magnetic shield were coaxially placed in the experimental chamber (Figure S4). The *Z*-axis was set in the direction parallel to the projectile trajectory. Before the shock remanence experiments, the basalt samples were subjected to a one-axial (*Z*-axis) AFD of 80 mT using a DEM-8601C AF demagnetizer (Natsuhara-Giken) comprising a large solenoid coil with a diameter of 12 cm.

Two SRM acquisition experiments were conducted under different applied field conditions (Table S1). An aluminum sphere with a diameter of 2 mm was used as the projectile, and a nylon slit sabot was used to accelerate the projectile (Kawai et al., 2010). The impact velocity was set to approximately 7 km/s, and the impact angle was fixed at 90°, measured from the top flat surface of the basalt cylinder. The magnetic fields of 0 and 100 μT were applied during the shock experiments, and the applied field direction under the 100 μT condition was a positive direction in the *Z*-axis. The spatial change in the magnetic field intensity around the basalt cylinder was below 4% (Figure S5).

2.3 Remanence measurement

After the SRM acquisition experiments, the target samples were cut into cubes using rock cutters. Slabs that were 3 mm thick and 24 mm wide were cut from the basalt cylinder. These were subsequently pasted on glass slides using a cyanoacrylate adhesive and divided into the oriented cube-shaped samples approximately 3 mm in length (Figure S6). The cube-shaped basalt and glass slide underneath were separated using acetone. Hereinafter, the cubic samples are denoted as R*i*Z*j*, where the indexes *i* and *j* are sample numbers from the impact point in the *R* and *Z* directions, respectively (Figure S6b). The magnetic field distribution around the rock cutters was measured using a Model 4048 Gauss Meter (F. W. BELL), and the field intensity was below 2 mT. Fifteen cube samples were cut from the unshocked basalt and the intensities of anhysteretic remanent magnetization (ARM) for these cube samples were imparted with DC and AC fields of 50 μT and 80 mT, respectively, to evaluate the inhomogeneity. The average and two standard deviations of the ARM intensity were 5.84×10^{-4} and 1.37×10^{-4} Am^2/kg, respectively; the inhomogeneity among the 3 mm cube samples was estimated to be 23%.

The remanence measurements were conducted using a Model 755 SQUID magnetometer (2G Enterprise) at the Center for Advanced Marine Core Research, Kochi University. An acrylonitrile butadiene styrene (ABS) sample holder and measurement methods specially designed for single crystal remanence measurements (Sato et al. 2015) were employed for the cube sample measurements. Stepwise AFD treatments up to 80 mT were conducted using a DEM-95C alternating field demagnetizer (Natsuhara-Giken) in the axial direction (*Z*-axis). After the SRM measurements, the ARM with DC and AC fields of 50 μT and 80 mT, respectively, was measured for the 12 cube samples to evaluate the change in magnetic properties. The cube samples selected for the magnetic measurements are shown in Figure S6b. Considering that the laboratory IRM is below 2 mT and the residual of the original NRM coercivity is higher than 80 mT, the remanence components of the coercivity ranging between 2–80 mT are characterized as the SRM components in this study.

2.4 Impact simulation

A series of impact simulations using the two-dimensional version of the iSALE shock physics code (Amsden et al., 1980; Ivanov et al., 1997; Wünnemann et al., 2006) was conducted to estimate the peak pressure P_{peak} and temperature T_{peak} values in the SRM acquisition experiments. The impact velocity and shapes of the projectile and target in the simulation were set to the same value achieved in the SRM acquisition experiments. The Tillotson EOS with parameters pertaining to aluminum (Tillotson, 1962) and the analytical equations of state (ANEOS, Thompson and Lauson, 1972) with parameters set for basalt were employed for the projectile and target, respectively. A parameter set of ANEOS for basalt was constructed by fitting the experimental data of Sekine et al. (2008) and listed in Table S4. The ROCK model in the iSALE package (Collins et al., 2004), with parameters set for basalt (Bowling et al., 2020), was employed to treat the elasto-plastic behavior in the basalt target. The end time of the simulation was set to the time taken for a generated compressional wave to sweep the entire target. Lagrangian tracer particles were inserted into each computational cell such that the pressure and temperature values in the simulation were stored on the tracers. The mass-weighted averaged values of the P_{peak} and T_{peak} in each 3 mm cube region were calculated to compare the calculated pressure and temperature changes with the experimentally measured SRM properties. Further details of the impact simulation are provided in the Supporting Information.

3. Results

A representative result for the stepwise AFD treatment of the SRM component is shown in Figure S7 as an orthogonal vector plot. The SRM component is confirmed to be a single component in one direction as they linearly decreased in all the cube samples. The average SRM directions deviated by 3° from the direction of the applied field and the 95% confidence limit (α_{95}) was estimated to be 3°. The SRM was likely aligned to the applied field direction, although the preliminary orienting method for the cube samples had a large orientation uncertainty.

The SRM intensity was calculated as $|\boldsymbol{J}_{2\ \mathrm{mT}} - \boldsymbol{J}_{80\ \mathrm{mT}}|$, where $\boldsymbol{J}_{\mathrm{X\ mT}}$ is the remanence vector at the X mT AFD step, and is plotted as a function of the distance from the impact point in Figure 1a. The SRM intensity in the case with a zero field shows an almost constant value (ranging from 0.06–0.89 × 10^{-4} $\mathrm{Am^2/kg}$ and an average of 0.40 × 10^{-4} $\mathrm{Am^2/kg}$) in a random direction. In contrast, the SRM intensity in the case with an applied field of 100 μT systematically changes with the distance; the maximum is at approximately 10–15 mm from the impact point, which subsequently decreases monotonically with increasing distance. The systematic change in the SRM intensity is also clear in the two-dimensional intensity map (Figure 1c). The SRM intensity in the case with an applied field of 100 μT is larger than that of zero, except for the two cube samples. Considering the inhomogeneities in the magnetic minerals among the 3 mm cube samples (23%) and applied field intensities during the SRM acquisition experiment (4%), it was confirmed that the basalt sample acquired the remanent magnetization as a result of shock wave propagation in an applied magnetic field of 100 μT.

A representative AFD curve for the SRM component of the cube sample in the case with an applied field of 100 μT is shown in Figure 2 with the AFD curves of 50 μT thermoremanent magnetization (TRM) and 500 mT IRM imparted for a 1-inch core basalt sample. The stability of the SRM component varies in the cube samples; the AFD curve of the SRM component was as stable as the TRM in one sample, while it was magnetically softer than the IRM in another sample. The stability of the SRM component was evaluated as $|\boldsymbol{J}_{14\ \mathrm{mT}}/\boldsymbol{J}_{2\ \mathrm{mT}}|$ and plotted as a function of the distance from the impact point in Figure 1b. A two-dimensional stability map of the SRM component is shown in Figure 1d. The stability monotonously decreased with increasing distance from the impact point (within approximately 15 mm), and likely converged 0.3–0.4 mm from the 15 mm.

The average and two standard deviations of the ARM intensity values for the selected cube samples were 5.73×10^{-4} and 0.88×10^{-4} $\mathrm{Am^2/kg}$, respectively. There was no significant difference between the ARM intensity values for the shocked and original samples, indicating that the magnetic properties of the basalt sample used in this study did not undergo alteration owing to the shock wave propagation.

The results of the impact simulations are illustrated as a two-dimensional map for the P_{peak} and T_{peak} values in Figures S11a and 11b. The target basalt sample experienced a P_{peak} ranging from 10 GPa near the impact point to below 0.1 GPa at the bottom of the basalt cylinder in the SRM acquisition experiment. A significant temperature rise was restricted to the region within 10 mm from the impact point, and the target basalt sample experienced a T_{peak} of up to 600 K in the region. The averaged P_{peak} of the cube sample monotonously increased with increasing average T_{peak} (Figure S12a).

4. Discussion

The SRM intensity and stability are plotted as functions of the average P_{peak} (Figure 3). When the P_{peak} ranges below 1.1 GPa, the SRM intensity linearly changes with the P_{peak}, while the samples with a P_{peak} higher than 1.9 GPa deviate from the linear trend. The cube samples showing the linear trend did not experience a temperature rise during the shock wave propagation (T_{peak} less than 315 K), while the deviating samples experienced a significant temperature change (T_{peak} values between 340–590 K). The P_{peak} dependence of the SRM intensity was calculated for the sample with a P_{peak} below 1.1 GPa that is given as

$$\frac{J_{SRM}}{Am^2kg^{-1}} = 3.50 \times 10^{-4} \times \frac{P_{peak}}{GPa} + 1.18 \times 10^{-4} \ (1),$$

where J_{SRM} is the SRM intensity. Assuming the proportionality in the applied field intensity, the efficiencies for the SRM acquisition are estimated to be 3.50 and 5.0×10^2 $Am^2kg^{-1}T^{-1}GPa^{-1}$ for the basalt and titanomagnetite contained in the basalt sample, respectively. The efficiency for the TRM acquisition is estimated to be 46.0 $Am^2kg^{-1}T^{-1}$, and the SRM acquisition efficiency when the P_{peak} is 1 GPa is 7.61% of that of the TRM. The intercept coefficient of 1.18×10^{-4} Am^2/kg in the linear regression is larger than the SRM intensity of the zero field. Although the SRM structure depends on the nature of the magnetic mineral (composition and domain state), the decreasing trend in the SRM intensity is consistent with the mixture of SD and MD titanomagnetite (Pohl et al., 1975) and MD titanomagnetite (Srnka et al., 1979), while the SRM properties were almost unchanged for the PSD titanomagnetite (Gattaccecca et al., 2008, 2010).

Regarding the origin of SRM observed in this study, multiple dominant factors can be described for the three different aspects: the constant J_{SRM} below 0.1 GPa, J_{SRM} proportional to the P_{peak} up to 1.1 GPa, and the J_{SRM} deviating from the linear trend above 1.9 GPa. The basalt sample used in this study did not experience the alteration of magnetic properties due to the shock wave propagation. This is consistent with previous studies showing that changes in magnetic properties after the shock experiment were distinct above 10 GPa (Gattacceca et al., 2007; Bezaeva et al., 2016). Thus, the above characteristics arose from the magnetically reversible changes during the shock wave propagation.

The linear trend up to 1.1 GPa likely arose from pressure effects. In the case of grains exhibiting uniaxial magnetic anisotropy under a uniaxial stress σ applied parallel to the easy direction of anisotropy, the uniaxial stress effect on the microcoercivity H_K is expressed as

$$H_K{}' = H_K - \frac{3\lambda_s\sigma}{\mu_0 M_s} = \frac{2K_u}{\mu_0 M_s} - \frac{3\lambda_s\sigma}{\mu_0 M_s} \quad (2),$$

where H_K' is the modified microcoercivity, λ_s is the averaged magnetostriction for randomly oriented crystals, μ_0 is the permeability of free space, M_s is the spontaneous magnetization, and $2K_u/\mu_0M_s$ expresses the microcoercivity due to uniaxial anisotropy (Dunlop and Özdemir, 1997). The uniaxial stress reduces the microcoercivity, although the magnitude of reduction varies with the relative orientations of the stress, magnetic field, and easy direction. The IRM-like AFD curves for the SRM of this region support this interpretation. The SRM is probably acquired as a result of the microcoercivity decrease/increase cycle due to the pressure increase/decrease cycle during the shock wave propagation. In-situ measurements of the magnetic properties of titanomagnetite, such as the magnetostriction constants (Nagata and Kinoshita, 1967) and coercivity (e.g., Gilder et al., 2004; Sato et al., 2015) are prospective future studies to confirm the acquisition mechanism.

The constant J_{SRM} value can be interpreted as the remanence component saturated at less than 0.1 GPa. The magnetoelastic anisotropy significantly contributes to the H_K in titanomagnetite with x = 0.6 (Dunlop and Özdemir, 1997) and is probably dominant for the titanomagnetite used in this study (x = 0.51). However, there might be a certain number of grains with dominating shape and magnetocrystalline anisotropy, and the microcoercivity of these grains reduce to almost zero during the uniaxial compression below 0.1 GPa, resulting in the saturation of their remanence.

The deviation from the linear trend apparently considers multiple factors. The sample of this region experienced a significant change in temperature (340–590 K). The SRM stability increases with increasing T_{peak} up to the TRM-like AFD curve, while the SRM intensity is almost unchanged or decreases slightly with increasing T_{peak}. This suggests that these remanences are distinctively different from the simple TRM. Considering the pressure effect on the T_C of titanomagnetite as ~15 K/GPa (Schult, 1970), M_s decreases with increasing temperature, while the elevating T_C due to increasing pressure reduces the temperature effect. Time series for the shape of the three-dimensional energy surface considering the relative orientations of the stress (both original and shock wave), magnetic field, and titanomagnetite grain should be calculated for temperature and pressure changes during the shock wave propagation in future studies to understand the origin of SRM for high pressure regions.

The SRM structure observed in this study has implications for the source of the magnetic anomaly observed over the Martian impact craters. There is a clear relationship between the formation ages of the Martian impact craters and the intensities of magnetic anomaly over the crater (Lillis et al., 2008). Additionally, the SD titanomagnetite could be a possible source of the Martian magnetic anomaly (Dunlop and Arkani-Hamed, 2005). Assuming that the SD titanomagnetite is the main remanence carrier of the Martian crust, the crustal rock acquired the SRM with varying intensities and stabilities at the time of impact. Subsequently, depending on the SRM stability, the SRM intensity relaxed after the impact, and its structure changed from the original distribution. The remanence relaxation tends to emphasize the magnetization around the crater center because of its high stability. However, a detailed relaxation calculation based on the magnetic properties of titanomagnetite (e.g., Sato et al., 2018) should be conducted in a future study. The three-dimensional distribution of the SRM intensity in the crust probably creates a unique spatial pattern of magnetic anomalies over the impact craters. Deciphering the magnetization distribution based on the experimentally constructed SRM distribution model can provide information on the paleo-planetary field evolution.

5. Conclusion

This study conducted SRM acquisition experiments and remanence measurements for cube-shaped subsamples using SD titanomagnetite-bearing basalt samples to understand the SRM intensity and stability structures. The SRM intensity and stability systematically change with distance from the impact point. In addition to the SRM experiments, impact simulations were conducted to estimate the pressure and temperature changes during the shock wave propagation and compare the calculated pressure and temperature changes with the observed SRM properties. Three distinctive aspects of SRM properties are recognized at different pressure ranges: (1) the SRM intensity is almost constant below 0.1 GPa, (2) the SRM intensity linearly increases with increasing pressure up to 1.1 GPa, and (3) the SRM intensity is almost constant, while the SRM stability increases with increasing pressure above 1.9 GPa. Regarding the SRM acquisition mechanisms, the pressure effect was likely dominant below 1.1 GPa, while multiple factors can be considered in the high-pressure range. The systematic changes in the SRM intensity and stability suggest that the crustal rocks containing the SD titanomagnetite had an SRM intensity structure at the time of impact, and this structure changed subsequently.

Acknowledgement

The authors wish to thank Dr. Haruka Ono for providing with the preliminary electron microscope measurement of the basalt sample. The authors thank the developers of iSALE, including G. Collins, K. Wünnemann, B. Ivanov, J. Melosh, and D. Elbeshausen. We used pySALEplot to analyze the output file of iSALE, and also thank Tom Davison for the development of pySALEPlot. This study was performed under the cooperative research program of Center for Advanced Marine Core Research (CMCR), Kochi University (Accept 18A038). Data from this paper are archived at the figshare (https://doi.org/10.6084/m9.figshare.13671322.v1). K.K. is supported by JSPS KAKENHI grants JP18H04464 and JP19H00726. The iSALE shock physics code is not fully open-source, but it is distributed on a case-by-case basis to academic users in the impact community for non-commercial use. A description of the application requirements can be found at the iSALE website (http://www.isale-code.de/redmine/projects/isale/wiki/Terms_of_use). The M-ANEOS

package has been available from Thompson SL, Lauson HS, Melosh HJ, Collins GS and Stewart, ST, M-ANEOS: A Semi-Analytical Equation of State Code, Zenodo, http://doi.org/10.5281/zenodo.3525030.

References

1. Acuña, M. H., Connerney, J. E. P., Lin, R. P., Mitchell, D., Carlson, C. W., McFadden, J., et al. (1999). Global distribution of crustal magnetization discovered by the Mars Global Surveyor MAG/ER experiment. Science, 284(5415), 790–793.
2. Amsden, A., Ruppel, H., and Hirt, C. (1980). SALE: A simplified ALE computer program for fluid flow at all speeds, Los Alamos National Laboratories Report, LA-8095:101p.
3. Bezaeva, N. S., Swanson-Hysell, N. L., Tikoo, S. M., Badyukov, D. D., Kars, M., Egli, R., et al. (2016). The effects of 10 to >160 GPa shock on the magnetic properties of basalt and diabase. Geochemistry, Geophysics, Geosystems, 17, 4753–4771.
4. Bowling, T. J., Johnson, B. C., Wiggins, S. E., Walton, E. L., Melosh, H. J., and

Sharp, T. G. (2020). Dwell time at high pressure of meteorites during impact ejection from Mars. Icarus, 343, 113689.

5. Collins, G. S., Melosh, H. J., and Ivanov, B. A. (2004). Modeling damage and deformation in impact simulations. Meteoritics and Planetary Science, 39, 217–231.

6. Day, R., M. Fuller, and V. A. Schmidt (1977), Hysteresis properties of titanomagnetites: Grain-size and compositional dependence, Phys. Earth Planet. Inter., 13, 260–267.

7. Dunlop, D. J., and Arkani-Hamed, J. (2005). Magnetic minerals in the Martian crust. Journal of Geophysical Research, 110, E12S04.

8. Dunlop, D. J., and Ö. Özdemir (1997), Rock Magnetism: Fundamentals and Frontiers, Cambridge University Press, 573 pp.

9. Gattacceca, J., A. Lamali, P. Rochette, M. Boustie, and L. Berthe (2007), The effects of explosive-driven shocks on the natural remanent magnetization and the magnetic properties of rocks, Phys. Earth Planet. Inter., 162, 85–98.

10. Gattacceca, J., L. Berthe, M. Boustie, F. Vadeboin, P. Rochette, and T. De

Resseguier (2008), On the efficiency of shock magnetization processes, Phys. Earth Planet. Inter., 166, 1–10.

11. Gattacceca, J., M. Boustie, E. Lima, B. P. Weiss, T. de Resseguier, and J.-P. Cuq-Lelandais (2010), Unraveling the simultaneous shock magnetization and demagnetization of rocks, Phys. Earth Planet. Inter., 182, 42–49.

12. Gilder, S., M. LeGoff, J.-C. Chervin, and J. Peyronneau (2004), Magnetic properties of single and multi-domain magnetite under pressures from 0 to 6 GPa, Geophys. Res. Lett., 31, L10612.

13. Hunt, C.P., Moskowitz, B.M., and Banerjee, S.K. (1995), Magnetic properties of rocks and minerals, in Rock Physics and Phase Relations: A Handbook of Physical Constants, Vol. 3, pp. 189–204, ed. Ahrens, T.J., American Geophysical Union.

14. Ivanov, B. A., Deniem, D., and Neukum, G. (1997). Implementation of dynamic strength models into 2-D hydrocodes: Applications for atmospheric breakup and impact cratering. International Journal of Impact Engineering, 20(1–5), 411–430.

15. Kawai, N., K. Tsurui, S. Hasegawa, and E. Sato (2010), Single microparticle launching method using two-stage light-gas gun for simulating hypervelocity

impacts of micrometeoroids and space debris, Rev. Sci. Instrum., 81, 115105.

16. Lillis, R. J., Frey, H. V., and Manga, M. (2008). Rapid decrease in Martian crustal magnetization in the Noachian era: Implications for the dynamo and climate of early Mars. Geophysical Research Letters, 35, L14203.

17. Mitchell, D. L., J. S. Halekas, R. P. Lin, S. Frey, L. L. Hood, M. H. Acuña, and A. Binder (2008), Global mapping of lunar crustal magnetic fields by Lunar Prospector, Icarus, 194, 401– 409.

18. Moskowitz, B.M., Jackson, M., and Kissel, C. (1998), Low-temperature mag- netic behavior of titanomagnetites, Earth planet. Sci. Lett., 157, 141–149.

19. Nagata, T. (1971), Introductory notes on shock remanent magnetization and shock demagnetization of igneous rocks, Pure Appl. Geophys., 89, 159–177.

20. Nagata, T., and H. Kinoshita (1967), Effect of hydrostatic pressure on magnetostriction and magnetocrystalline anisotropy of magnetite, Phys. Earth Planet. Inter., 1, 44–48.

21. Pohl, J., U. Bleil, and U. Hornemann (1975), Shock magnetization and demagnetization of basalt by transient stress up to 10 kbar, J. Geophys., 41, 23–41.

22. Roberts, A. P., C. R. Pike, and K. L. Verosub (2000), First-order reversal curve diagrams: A new tool for characterizing the magnetic properties of natural samples, J. Geophys. Res., 105, 28,461–28, 475.

23. Sato, M., S. Yamamoto, Y. Yamamoto, Y. Okada, M. Ohno, H. Tsunakawa, and S. Maruyama (2015), Rock-magnetic properties of single zircon crystals sampled from the Tanzawa tonalitic pluton, central Japan, Earth Planets Space, 67, 150.

24. Sato, M., Yamamoto, Y., Nishioka, T., Kodama, K., Mochizuki, N., Usui, Y., and Tsunakawa, H. (2015). Pressure effect on magnetic hysteresis parameters of single-domain magnetite contained in natural plagioclase crystal. Geophysical Journal International, 202(1), 394–401.

25. Sato, M., Yamamoto, Y., Nishioka, T., Kodama, K., Mochizuki, N., Ushioda, M., Nakada, R., and Tsunakawa, H. (2018) Constraints on the source of the Martian magnetic anomalies inferred from relaxation time of remanent magnetization. Geophysical Research Letters, 45, 6417–6427.

26. Schult, A. (1970). Effect of pressure on the Curie temperature of titanomagnetites [(1−x)·Fe3O4−x·TiFe2O4]. Earth and Planetary Science Letters, 10(1), 81–86.

27. Sekine, T., T. Kobayashi, M. Nishio, and E. Takahashi (2008), Shock equation of state of basalt, Earth Planets Space, 60, 999–1003.

28. Srnka, L., G. Martelli, G. Newton, S. Cisowski, M. Fuller, and R. Schaal (1979), Magnetic field and shock effects and remanent magnetization in a hypervelocity impact experiment, Earth Planet. Sci. Lett., 42, 127–137.

29. Thompson, S. L., and H. S. Lauson (1972), Improvements in the Chart-D radiation hydrodynamic code III: Revised analytical equation of state, pp. SC-RR-71 0714 119 pp., Sandia Laboratories, Albuquerque, NM.

30. Tillotson, J. H. (1962). Metallic equations of state for hypervelocity impact Rep., 141 pp, DTIC Document.

31. Wünnemann, K., Collins, G. S., and Melosh, H. J. (2006). A strain-based porosity model for use in hydrocode simulations of impacts and implications for transient crater growth in porous targets. Icarus, 180(2), 514–527.

Figures

Figure 1. Shock remanence (a) intensity and (b) stability plotted as a function of

distance from the impact point. Two-dimensional structure map for the shock remanence (c) intensity and (d) stability.

Figure 2. Stepwise alternating field demagnetization (AFD) curves for shock remanences. Normalized remanence intensity is plotted as a function of applied AF field peak. AFD curves of the thermoremanent magnetization (TRM) and isothermal remanent magnetization (IRM) are shown in grey lines.

Figure 3. Shock remanence (a) intensity and (b) stability plotted as a function of peak pressure during the shock wave propagation. Grey circles indicate that the sample is subjected to peak pressure higher than 1.9 GPa. Dashed line in (a) shows a linear regression line for the sample subjected to peak pressure below 1.1 GPa.

Figure 1.

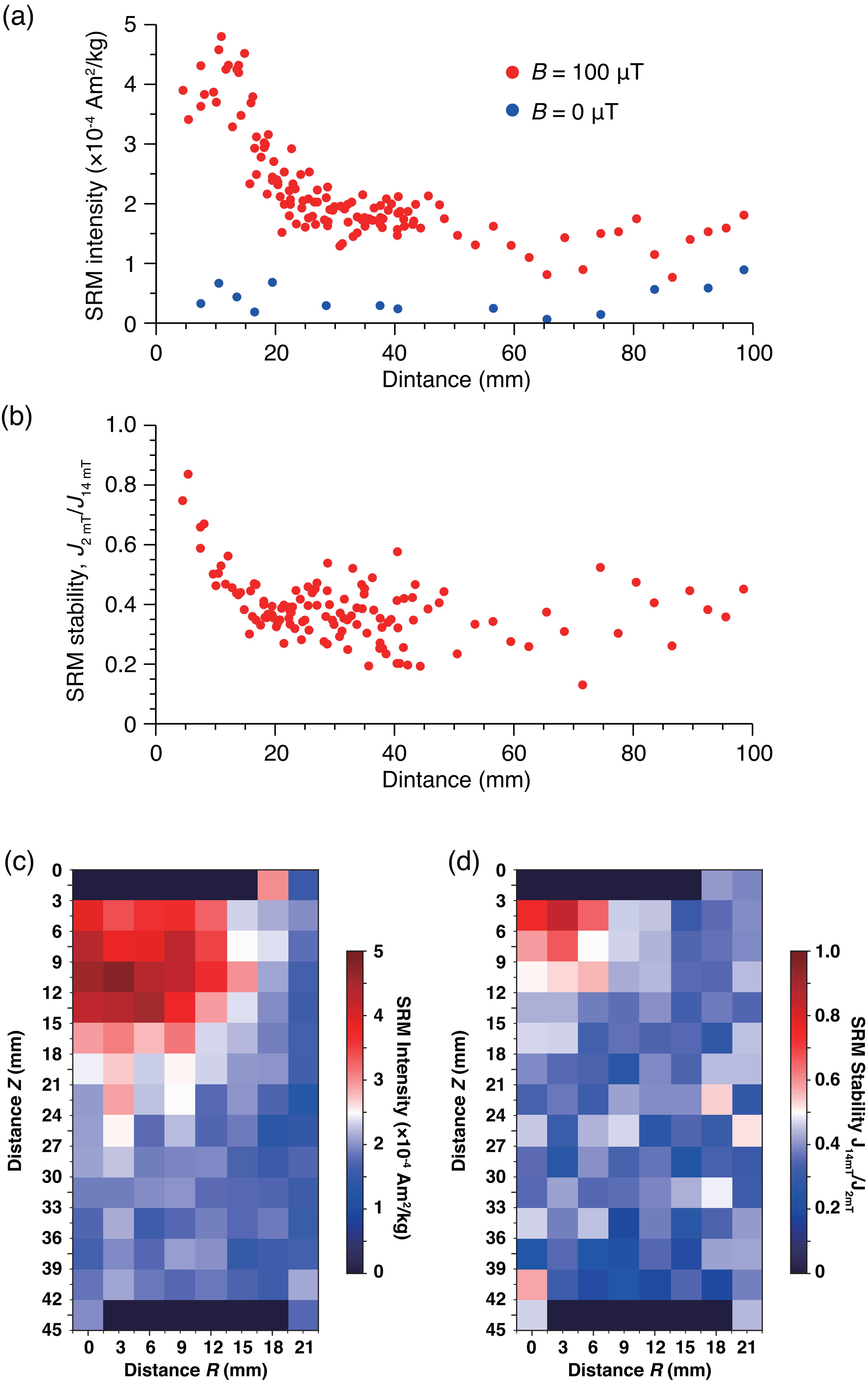

(a)
SRM intensity (×10⁻⁴ Am²/kg)
B = 100 μT
B = 0 μT
Dintance (mm)
(b)
SRM stability, J2 mT/J14 mT
Dintance (mm)
(c)
Distance Z (mm)
Distance R (mm)
SRM Intensity (×10⁻⁴ Am²/kg)
(d)
Distance Z (mm)
Distance R (mm)
SRM Stability J14mT/J2mT

Figure 2.

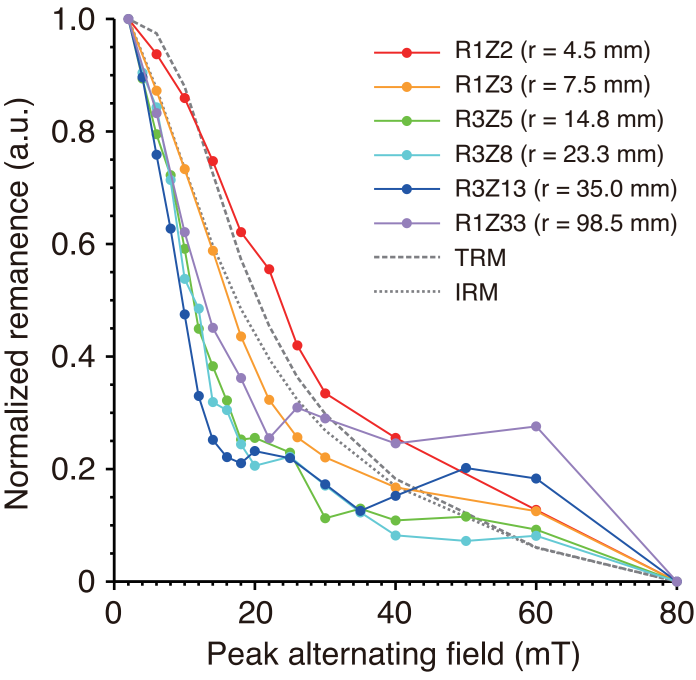

1.0
0.8
0.6
0.4
0.2
0
Normalized remanence (a.u.)
0
20
40
60
80
Peak alternating field (mT)
R1Z2 (r = 4.5 mm)
R1Z3 (r = 7.5 mm)
R3Z5 (r = 14.8 mm)
R3Z8 (r = 23.3 mm)
R3Z13 (r = 35.0 mm)
R1Z33 (r = 98.5 mm)
TRM
IRM

Figure 3.

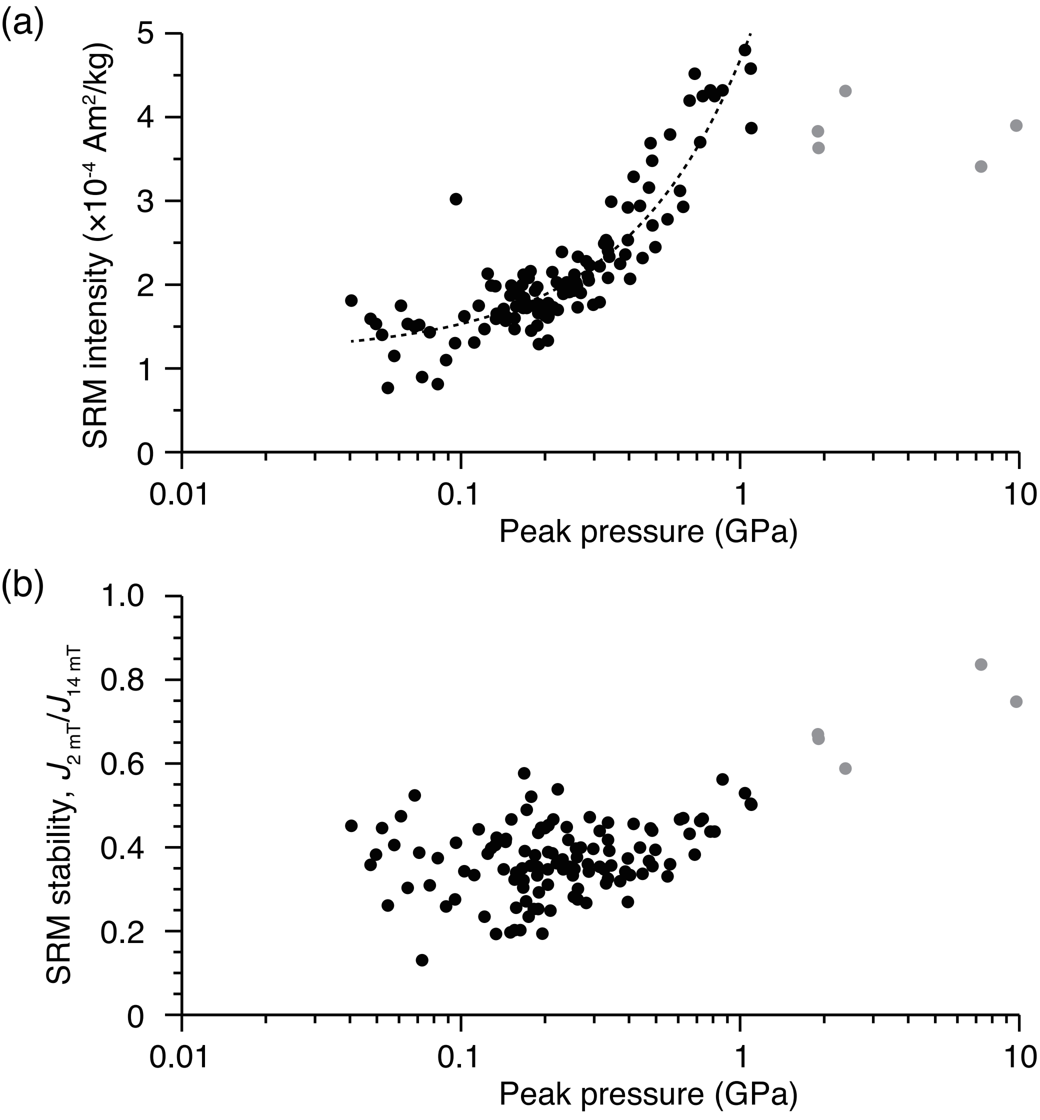

(a)
SRM intensity (×10⁻⁴ Am²/kg)
0
1
2
3
4
5
0.01
0.1
1
10
Peak pressure (GPa)
(b)
SRM stability, $J_{2\,mT}/J_{14\,mT}$
0
0.2
0.4
0.6
0.8
1.0
0.01
0.1
1
10
Peak pressure (GPa)